Gauge angle dependence in TDHFB calculations of ^{20}O + ^{20}O head-on collisions with the Gogny interaction

Yukio Hashimoto*

Center for Computational Sciences, University of Tsukuba, Tsukuba 305-8571, Japan

Guillaume Scamps†

Department of Physics, Tohoku University, Sendai 980-8578, Japan

Abstract

A numerical method to solve the TDHFB equations by using a hybrid basis of the two-dimensional harmonic oscillator eigenfunctions and one-dimensional Lagrange mesh with the Gogny effective interaction is applied to the head-on collisions of the superfluid nuclei ^{20}O's. Taking the energies around the barrier top, the trajectories, pairing energies, and numbers of transferred nucleons are displayed. Their dependence on the relative gauge angle at the initial time is studied.

1 Introduction

The nuclear superfluidity has attracted continuous attention among the nuclear physicists for more than fifty years. The structure of the nuclear ground states, the reaction mechanism of a pair of colliding nuclei, the dynamical properties of the fission processes, and so on, have been studied in connection with the pairing correlations among the nucleons in the nucleus (nuclei) [1, 2, 3, 4, 5].

The time-dependent mean-field theory has been one of the useful theoretical frameworks to study the static as well as dynamical properties of the nuclei. The time-dependent Hartree-Fock (TDHF) method is the foremost example of the time-dependent mean-field methods. The TDHF has been widely in use in the investigations of the small-amplitude collective vibrations around the ground states as well as the large-amplitude collective motions in the nuclear

---

*hashimoto.yukio.gb@u.tsukuba.ac.jp
†scamps@nucl.phys.tohoku.ac.jp

1

fusion/fission processes [6, 7, 8, 9, 10, 11, 12, 13, 14, 15]. The TDHF has been extended to deal with the effects of the pairing correlation into the time-dependent Hartree-Fock Bogoliubov (TDHFB) or TDHF+BCS methods [16, 17, 18, 19, 20, 21, 22].

In relation with the reaction processes of two superfluid nuclei, one of the long-standing, interesting subjects is to make clear the mechanism of the particle transfer phenomena influenced by the pairing correlation in the sub-barrier energy region. The particle transfer process between the two superfluid nuclei may be analogous to the *Josephson effect* in the solid state physics [23, 24]. In the Josephson effect, the electric current flows between the two superconducting objects separated by a thin insulator in proportion to the sine of the difference of the phases of the superconducting objects.

In the mean-field framework of the BCS approximation or Hartree-Fock Bogoliubov (HFB) method, the ground state of the superfluid nucleus is accompanied by a time-dependent phase (gauge angle) whose angular velocity is the chemical potential. The phase has no effects on the ground state property of the nucleus, or on its evolution with the TDHFB equations of motion. In the collision process of two superfluid nuclei, the phase of the one nucleus could be different from that of the other's. In order to make clear the mechanism of the nuclear Josephson effect [25, 26, 27, 28, 29, 30], we propose to study the effects of the difference of the phases (relative phase) between the two initial nuclei.

Recently, several groups have calculated the numbers of the transferred nucleons in the nuclear collisions by making use of the quantum mechanical method of the number projection, in which the angular variables are used as the generator coordinates (integration variables) [22, 31, 32, 33]. In the framework of the mean-field calculations of the TDHFB, additional effects of the relative phase is expected on the physical quantities such as trajectories, pairing energies, potential profiles, and so on, in the collision processes.

In this article, we propose a numerical technique of solving the TDHFB equations by using the hybrid basis of the two-dimensional harmonic oscillator eigenfunctions and one-dimensional Lagrange mesh [21]. Then, we report its first application to the head-on collision processes of the superfluid oxygens ^{20}O's. We study the effects of the relative gauge angle of two colliding nuclei by adopting four different angles (0, 45, 90, and 135 degrees) as the representative samples. The dependence of the potentials between the colliding nuclei, trajectories, and pairing energies on the relative phase are discussed.

This article is composed of the following sections: In Section II, the TDHFB equations are given together with the initial conditions of the two colliding superfluid nuclei. In Section III, the TDHFB calculations of the collision processes of the two oxygens ^{20}O's are carried out with the three values of the boost energies, $E_{\mathrm{boost}} = 4.8$, 5.0, and 5.2 MeV, leading to the center-of-mass energy $E_{\mathrm{c.m.}} = 9.21$, 9.41, and 9.61 MeV, respectively. The trajectories, pairing energies, and the number of the transferred nucleons are displayed. In Section IV, the effects of the initial relative phase (gauge angle) are discussed. Section V is for the summary and concluding remarks.

2 Basic equations and initial conditions

2.1 Basic equation

The nuclear Hamiltonian under consideration is in the form,

$$H = \sum_{\alpha\beta} T_{\alpha\beta} C_\alpha^\dagger C_\beta + \frac{1}{4} \sum_{\alpha\beta\gamma\delta} \mathcal{V}_{\alpha\beta\gamma\delta} C_\alpha^\dagger C_\beta^\dagger C_\delta C_\gamma, \tag{1}$$

where $T_{\alpha\beta}$ is the kinetic energy matrix element and $\mathcal{V}_{\alpha\beta\gamma\delta}$ is the antisymmetrized two-body matrix element of the Gogny interaction. The operator $C_\alpha^\dagger (C_\alpha)$ is a nucleon creation (annihilation) operator of a state labelled with α.

The quasi-particles $\beta_k^{(\tau)\dagger}$ and $\beta_k^{(\tau)}$ are introduced by the Bogoliubov transformation from the particle operators $C_\alpha^\dagger$ and C_α,

$$\beta_k^{(\tau)\dagger} = \sum_\alpha \left(U_{\alpha k}^{(\tau)} C_\alpha^\dagger + V_{\alpha k}^{(\tau)} C_\alpha \right), \tag{2}$$

$$\beta_k^{(\tau)} = \sum_\alpha \left(U_{\alpha k}^{(\tau)*} C_\alpha + V_{\alpha k}^{(\tau)*} C_\alpha^\dagger \right), \tag{3}$$

where $\tau = $ p (n) for protons (neutrons), respectively.

In the TDHFB method, the equations of motion for the matrices $U^{(\tau)}$ and $V^{(\tau)}$ in the Bogoliubov transformation (2) and (3) are given in the form [16, 20],

$$i\hbar \frac{\partial}{\partial t} \left(\begin{array}{c} U^{(\tau)}(t) \\ V^{(\tau)}(t) \end{array} \right) = \mathcal{H}^{(\tau)} \left(\begin{array}{c} U^{(\tau)}(t) \\ V^{(\tau)}(t) \end{array} \right), \tag{4}$$

with the HFB Hamiltonian $\mathcal{H}^{(\tau)}$,

$$\mathcal{H}^{(\tau)} = \left(\begin{array}{cc} h^{(\tau)} & \Delta^{(\tau)} \\ -\Delta^{(\tau)*} & -h^{(\tau)*} \end{array} \right). \tag{5}$$

The mean field Hamiltonian $h^{(\tau)}$ and the pairing mean field $\Delta^{(\tau)}$ are introduced through the relations [2],

$$h_{\alpha\beta}^{(\tau)} = T_{\alpha\beta} + \Gamma_{\alpha\beta}^{(\tau)}, \tag{6}$$

$$\Gamma_{\alpha\beta}^{(\tau)} = \sum_{\gamma\delta} \mathcal{V}_{\alpha\gamma\beta\delta} \rho_{\delta\gamma}^{(\tau)}, \quad \Delta_{\alpha\beta}^{(\tau)} = \frac{1}{2} \sum \mathcal{V}_{\alpha\beta\gamma\delta} \kappa_{\gamma\delta}^{(\tau)}, \tag{7}$$

where $\rho^{(\tau)}$ and $\kappa^{(\tau)}$ are normal density matrix and pairing tensor,

$$\rho_{\alpha\beta}^{(\tau)} = \left(V^{(\tau)*} V^{(\tau)T} \right)_{\alpha\beta}, \quad \kappa_{\alpha\beta}^{(\tau)} = \left(V^{(\tau)*} U^{(\tau)T} \right)_{\alpha\beta}, \tag{8}$$

respectively. The symbol T in Eq. (8) stands for the transpose of a matrix.

As the basis functions labeled with $\alpha, \beta, \cdots$, we make use of the spatial grid points, i.e., the Lagrange mesh [34, 35] in the direction of the z axis, while the

two-dimensional harmonic oscillator eigen functions are used in the directions of the x and y axes [21].

The HFB matrices $U_{\alpha k}^{(\tau)}{}^{(0)}$ and $V_{\alpha k}^{(\tau)}{}^{(0)}$ of the ground state of a nucleus are obtained by solving the HFB equations [2],

$$
\begin{pmatrix} h^{(\tau)} - \lambda^{(\tau)} & \Delta^{(\tau)} \\ -\Delta^{(\tau)*} & -h^{(\tau)*} + \lambda^{(\tau)} \end{pmatrix} \begin{pmatrix} U_k^{(\tau)} \\ V_k^{(\tau)} \end{pmatrix}
$$
$$
= E_k^{(\tau)} \begin{pmatrix} U_k^{(\tau)} \\ V_k^{(\tau)} \end{pmatrix}, \tag{9}
$$

with the eigenvalues $E_k^{(\tau)}$ and a chemical potential $\lambda^{(\tau)}$. In Eq. (9), $U_k^{(\tau)}$ ($V_k^{(\tau)}$) denotes the vector $U_{\alpha k}^{(\tau)}$ ($V_{\alpha k}^{(\tau)}$) corresponding to the eigenvalue $E_k^{(\tau)}$ of the quasi-particle with a label k, respectively.

The inclusion of the chemical potential or any real variable μ in the mean-field Hamiltonians $h^{(\tau)} - \mu$ and $-h^{(\tau)*} + \mu$ in Eq. (5) will keep unchanged the evolution of the one-body density matrix $\rho^{(\tau)}$ and two-body correlation matrix $\kappa^{(\tau)}\kappa^{(\tau)*}$.

2.2   Initial conditions

When we set up the initial condition of the TDHFB equation (4), we assume that the two nuclei are uncorrelated and independent of each other if the distance between the two nuclei is large enough. With the purpose of realizing the situation, we make use of a Lagrange mesh whose number of the grid points N_{grid} is just the double of that of the original Lagrange mesh $N_{\text{grid}}^{(0)}$ (Fig. 1): $N_{\text{grid}} = 2 \times N_{\text{grid}}^{(0)}$.

In the left (L) region with negative z ($z < 0$) in the doubled Lagrange mesh (b) in Fig. 1), the HFB matrices $U_{\alpha k}^{(\tau)}{}^{(0)}$ and $V_{\alpha k}^{(\tau)}{}^{(0)}$ of the ground state solution on the Lagrange mesh (a) in Fig. 1) are mapped into the matrices $U_{\alpha k}$ and $V_{\alpha k}$ on the doubled Lagrange mesh,

$$
W_{\alpha k}^{(\tau)} = \begin{cases} W_{\alpha k}^{(\tau)}{}^{(0)}, & \alpha = 1, 2, \cdots, N_{\text{base}}/2, \\ 0, & \alpha = N_{\text{base}}/2 + 1, \cdots, N_{\text{base}}, \end{cases} \tag{10}
$$

where $k = 1, 2, \cdots, N_{\text{base}}/2$ and $W^{(\tau)}(W^{(\tau)}{}^{(0)})$ stands for the matrix $U^{(\tau)}(U^{(\tau)}{}^{(0)})$ or $V^{(\tau)}(V^{(\tau)}{}^{(0)})$, respectively. Here, N_{base} is the total number of the basis functions of the two-dimensional harmonic oscillator eigenfunctions and Lagrange mesh together with the spin degrees of freedom.

Just in the same way, in the right (R) region with positive z ($0 < z$) in the doubled Lagrange mesh, we have the mapped matrices $U_{\alpha k}^{(\tau)}$ and $V_{\alpha k}^{(\tau)}$,

$$
W_{\alpha k}^{(\tau)} = \begin{cases} 0, & \alpha = 1, 2, \cdots, N_{\text{base}}/2, \\ W_{\alpha' k}^{(\tau)}{}^{(0)} \; (\alpha' = \alpha - N_{\text{base}}/2), & \alpha = N_{\text{base}}/2 + 1, \cdots, N_{\text{base}}, \end{cases} \tag{11}
$$

4

where $k = N_{\text{base}}/2 + 1, \cdots, N_{\text{base}}$ and $W^{(\tau)}(W^{(\tau)(0)})$ is used for the matrix $U^{(\tau)}(U^{(\tau)(0)})$ or $V^{(\tau)}(V^{(\tau)(0)})$, respectively.

Note that this initialization method conserves the fermion commutation relations [2],

$$U^{(\tau)\dagger}U^{(\tau)} + V^{(\tau)\dagger}V^{(\tau)} = 1, \tag{12}$$

$$U^{(\tau)}U^{(\tau)\dagger} + V^{(\tau)*}V^{(\tau)T} = 1, \tag{13}$$

$$U^{(\tau)T}V^{(\tau)} + V^{(\tau)T}U^{(\tau)} = 0, \tag{14}$$

$$U^{(\tau)}V^{(\tau)\dagger} + V^{(\tau)*}U^{(\tau)T} = 0. \tag{15}$$

Each of the two nuclei is boosted with a momentum so that the total momentum of the system is zero and the initial position of the center-of-mass is kept at the initial point.
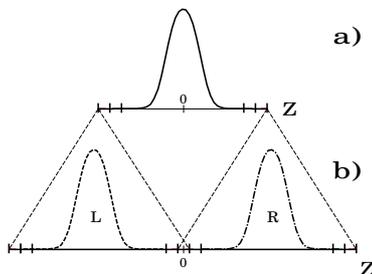
Figure 1: Initial condition of the TDHFB equation (4). A HFB ground state is calculated by using the basis functions with the number of the grid points $N_{\text{grid}}^{(0)} = N_{\text{grid}}/2$ (a)). The HFB ground state in a) is mapped on the space of the basis functions with the number of the grid points N_{grid} (L or R in b)).

3   Head-on collisions of two ^{20}O's

In the present calculations, the Gogny D1S is used as the effective interaction. We note that the Coulomb force is used only in the mean-field part and is not included in the pairing part of the HFB Hamiltonian.

The parameters used in the calculations are as follows: The grid spacing $\Delta z = 0.91$ fm and the total number of the grid points of the doubled Lagrange mesh N_{grid} is forty six. The harmonic oscillator eigenfunctions are used as the basis functions in the x-y plane. The space of the harmonic oscillator quantum number is restricted as $n_x + n_y \leq N_{\text{shell}} = 4$ with the quantum number n_x (n_y) in the direction of the x (y) axis, respectively. The total number of the basis functions N_{base} is $N_{\text{base}} = (N_{\text{shell}} + 1)(N_{\text{shell}} + 2)N_{\text{grid}}$ including spin up and down. The harmonic oscillator parameter $\hbar\omega = 14.6$ MeV and the maximum

number N_{shell} are used in the calculations of the HFB ground state solutions (a) in Fig. 1) as well as the head-on collisions of the two nuclei on the doubled mesh space (b) in Fig. 1) .

Here, we note that the restricted space limits the number of the degrees of freedom to 2760 including spin and isospin while a full calculation in Cartesian mesh would involve around 10^5 degrees of freedom. The CPU time for the one step of the integration of the TDHFB equations is four minutes on HITACHI SR16000M1 by using 512 CPUs. The one trajectory in the subsequent calculations is carried out in eight to ten days.
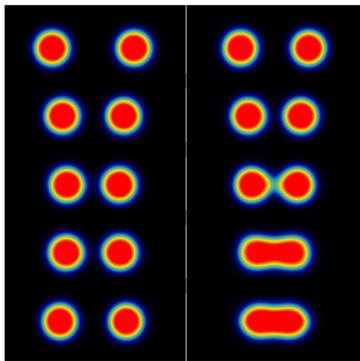
Figure 2: Densities in the yz plane in the collisions ^{20}O + ^{20}O for the center-of-mass energies $E_{\text{c.m.}}$=9.21 MeV (left) and $E_{\text{c.m.}}$=9.61 MeV (right). The densities are shown with respect to the time at the times $ct = 180, 360, 540, 720,$ and 900 fm from the top to the bottom, respectively. c is the light speed.

3.1 Relative distance, relative momentum, and transferred number of particle

The evolution of the system is shown in Fig. 2 for the two center-of-mass energies $E_{\text{c.m.}}$, where one is below the barrier and another is above the barrier. For the energy $E_{\text{c.m.}}$ below the barrier top, the two nuclei exchange nucleons and separate into two fragments, while the two nuclei merge into one for the energy $E_{\text{c.m.}}$ above the barrier top.

In order to understand the dynamical properties of the collision processes around the barrier, we followed Washiyama's method of introducing a section plane at a point on the z axis between the two colliding nuclei [12]. The section plane is set at the point $z = z_{\text{s}}$ where the density $\tilde{\rho}_{\text{L}}(\mathbf{r}, t)$ is equal to the density $\tilde{\rho}_{\text{R}}(\mathbf{r}, t)$. Here, $\tilde{\rho}_{\text{L/R}}(\mathbf{r}, t)$ is the density which started from the nucleus in the left (L) (right (R)) region,

$$\tilde{\rho}_{\text{L/R}}(\mathbf{r}, t) = \sum_{\alpha\beta} \Phi_\alpha(\mathbf{r})\Phi_\beta^*(\mathbf{r})\tilde{\rho}_{\alpha\beta}^{\text{L/R}}\delta_{\sigma_\alpha\sigma_\beta}, \tag{16}$$

6

with the density matrix $\tilde{\rho}_{\alpha\beta}^{L/R}$,

$$\tilde{\rho}_{\alpha\beta}^{L/R} = \sum_{\tau = p,n} \sum_{k'} V_{\alpha k'}^{(\tau)*} V_{\beta k'}^{(\tau)}, \tag{17}$$

respectively. The index k' takes the values $k' = 1, 2, \cdots, N_{base}/2$ for the $\tilde{\rho}_{\alpha\beta}^{L}$ and $k' = N_{base}/2 + 1, N_{base}/2 + 2, \cdots, N_{base}$ for the $\tilde{\rho}_{\alpha\beta}^{R}$. In (16), $\Phi_{\alpha}(\mathbf{r})$ and $\Phi_{\beta}(\mathbf{r})$ are the basis functions of the two-dimensional harmonic oscillator eigen functions and Lagrange mesh [21], and σ_{α} and so on are the labels of the spin.

Making use of the section plane at $z = z_s$, we calculated the number of the nucleons in each of the left region and right region with respect to the plane,

$$m_L = \int d^3x \, \rho(\mathbf{r})\theta(z_s - z), \tag{18}$$

$$m_R = \int d^3x \, \rho(\mathbf{r})\theta(z - z_s), \tag{19}$$

with the total density $\rho(\mathbf{r}) = \rho^{(p)}(\mathbf{r}) + \rho^{(n)}(\mathbf{r})$ made from the proton (p) and neutron (n) densities.

The center-of-mass position z_L (z_R) and momentum p_L (p_R) in the left (right) region divided by the section plane are calculated,

$$z_L = \mathrm{Tr}\left[(z)^{(L)}\rho\right]/m_L, \quad z_R = \mathrm{Tr}\left[(z)^{(R)}\rho\right]/m_R, \tag{20}$$

and

$$p_L = \mathrm{Tr}\left[(p_z)^{(L)}\rho\right], \quad p_R = \mathrm{Tr}\left[(p_z)^{(R)}\rho\right], \tag{21}$$

respectively. In Eqs. (20) and (21), the notation Tr is the trace of a matrix, and the notations $(z)^{(L)}$, $(z)^{(R)}$, $(p_z)^{(L)}$ and $(p_z)^{(R)}$ stand for the matrices with the matrix elements,

$$(z)_{\alpha\beta}^{(L)} = \int d^3x \, \theta(z_s - z)\Phi_{\alpha}(\mathbf{r})^* z\Phi_{\beta}(\mathbf{r})\delta_{\sigma_\alpha \sigma_\beta},$$

$$(p_z)_{\alpha\beta}^{(L)} = \int d^3x \, \theta(z_s - z)\Phi_{\alpha}(\mathbf{r})^* \left(-i\hbar\frac{\partial}{\partial z}\right) \Phi_{\beta}(\mathbf{r})\delta_{\sigma_\alpha \sigma_\beta}, \tag{22}$$

$$(z)_{\alpha\beta}^{(R)} = \int d^3x \, \theta(z - z_s)\Phi_{\alpha}(\mathbf{r})^* z\Phi_{\beta}(\mathbf{r})\delta_{\sigma_\alpha \sigma_\beta},$$

$$(p_z)_{\alpha\beta}^{(R)} = \int d^3x \, \theta(z - z_s)\Phi_{\alpha}(\mathbf{r})^* \left(-i\hbar\frac{\partial}{\partial z}\right) \Phi_{\beta}(\mathbf{r})\delta_{\sigma_\alpha \sigma_\beta}. \tag{23}$$

Here, ρ is the total density matrix $\rho = \rho^{(p)} + \rho^{(n)}$. The relative coordinate R and relative momentum P_z are defined,

$$\begin{aligned} R &= z_R - z_L, \\ P_z &= (m_L p_R - m_R p_L)/(m_L + m_R). \end{aligned} \tag{24}$$

3.2 Trajectories, pairing energies, and number of the transferred particles

As the examples of the head-on collisions of the two ^{20}O's, we chose three boost energies $E_{\text{boost}} = 4.8$ MeV, 5.0 MeV, and 5.2 MeV, leading to the center-of-mass energies $E_{\text{c.m.}} = 9.21$, 9.41, and 9.61 MeV, respectively.

In Fig. 3, we display the frozen density potential $V_{\text{FD}}(R)$ with respect to the relative distance R together with the positions of the three initial energies to show that they are below, nearly on, and above the top of the frozen density potential, respectively.
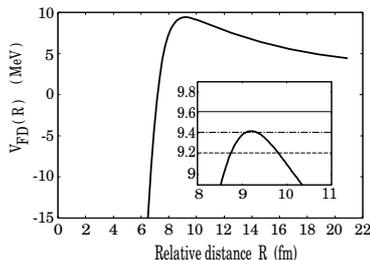
Figure 3: The frozen density potential $V_{\text{FD}}(R)$ with respect to relative coordinate R of the head-on collision of two ^{20}O's. The inset figure is the magnification of the region around the top of the frozen density potential. In the inset figure, three energies are described with broken, chain, and solid lines for $E_{\text{c.m.}} = 9.21$, 9.41, and 9.61 MeV, respectively.

Corresponding to the three energies $E_{\text{c.m.}}$, we got three trajectories of the colliding oxygens ^{20}O's in the phase space $R - P_z$ of the relative distance R and the relative momentum P_z.

In Fig. 4, we display the three trajectories in the phase space $R - P_z$. They start at $R = 20.91$ fm and follow each other side by side till they come around $R \sim 12$ fm. After passing the point around $R \sim 12$ fm, the three trajectories begin to separate from each other: The trajectory with the energy $E_{\text{c.m.}} = 9.21$ MeV corresponds to a process in which the two oxygens ^{20}O's come near each other, stop at the turning point around $R \sim 10$ fm, and then bounce back into the two fragments that are mixture of the components including the transfer states, the two initial ^{20}O's states in their ground states, and in their excited states.

The two trajectories with the energies $E_{\text{c.m.}} = 9.41$ MeV and 9.61 MeV, on the other hand, represent the process of fusion of the two nuclei after slowing down in the relative motion. The combined systems display vibration after the fusion of the two ^{20}O's in both cases of these energies.

In Fig. 5, the variations of the pairing energies along the three trajectories in Fig. 4 are displayed. We see that the pairing energies are kept almost constant before the two nuclei come to the region of the top of the potential energy
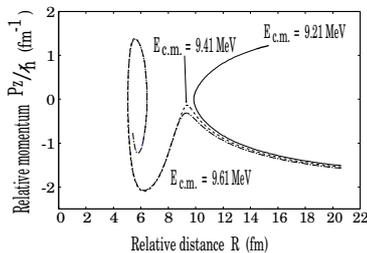
8

Figure 4: Trajectories in the phase space of the relative coordinate R and the relative momentum P_z. The curve in solid (broken, chain) corresponds to the initial energy $E_{\text{c.m.}} = 9.21$ (9.41, 9.61) MeV, respectively. The two trajectories with $E_{\text{c.m.}} = 9.41$ and 9.61 MeV almost fully overlap in the region $R < 8.5$ fm.

$V_{\text{FD}}(R)$ at around $R \sim 9.2$ fm for the cases of the energies $E_{\text{c.m.}} = 9.41$ MeV and 9.61 MeV. In a similar way, the pairing energy is kept almost constant until the two nuclei come to the turning point at around $R \sim 10.0$ fm for the case with the energy $E_{\text{c.m.}} = 9.21$ MeV.

Once the two nuclei begin to fuse in the cases of the energies $E_{\text{c.m.}} = 9.41$ and 9.61 MeV, the pairing energy E_{pair} rapidly becomes small in the magnitude from -13 MeV to -2 MeV, and oscillates around the value $E_{\text{pair}} \sim -2$ MeV in each case of the energies (a) and b) in Fig. 5). We can interpret this diminution of the pairing energy from the increase of the excitation energy after the fusion. The occurrence of the internal excitations is expected to reduce the pairing correlation. When the two nuclei turn back from the turning point (c) in Fig. 5), on the other hand, the variation of the pairing energy is 0.15 MeV.

In relation with the variations of the pairing energies in Fig. 5, let us calculate the numbers of the transferred nucleons. We followed the Washiyama's definition of the number of the transferred nucleons $N_{\text{trans}}^{\text{L/R}}[R(t)]$ in the collision process of a pair of the identical nuclei, which was used in the framework of the TDHF [12],

$$N_{\text{trans}}^{\text{L}}[R(t)] = \int d^3 x \tilde{\rho}_{\text{L}}(\mathbf{r}, t)\theta(z), \tag{25}$$

where L stands for the left nuclei at the initial time $t = 0$ and the density $\tilde{\rho}_{\text{L/R}}(\mathbf{r}, t)$ is given in (17). We paid attention only to the transfer of the nucleons which were in the left nuclei at the initial time, since the present system of two oxygen nuclei ^{20}O's is symmetric with respect to the origin $z = 0$. Then, the section plane is also put at the origin $z_s = 0$.

In Figs. 6 and 7, we show the transferred numbers of the protons and neutrons with respect to the relative distance R in the cases of the trajectories with the energies $E_{\text{c.m.}} = 9.61$ MeV and 9.21 MeV, respectively.

In Fig. 6, the two nuclei are in the process of the fusion within the region $R \leq 9.2$ fm, and the transferred numbers of the protons and neutrons rapidly increase
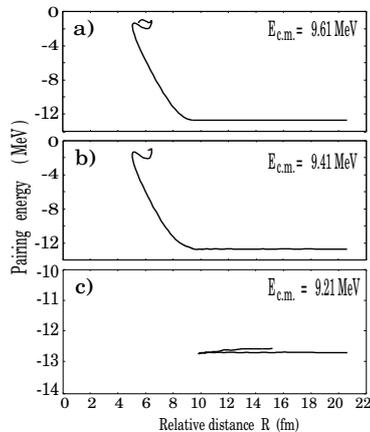
9

Figure 5: Pairing energies of the trajectories with the energies $E_{\mathrm{c.m.}} = 9.61$ MeV (a)), 9.41 MeV (b)), and 9.21 MeV (c)) are plotted with respect to the relative distance R.

as the overlap of the two nuclei becomes larger. In the figure, multiplying the transferred number of the protons by 1.5, we get a curve which goes along the curve of the number of the transferred neutrons. Since the value 1.5 is just the number of the N/Z ratio in the ^{20}O, we see that the protons and neutrons begin to move into the region of the other nuclei in a similar way after the combined system passes over the top of the potential energy $V_{\mathrm{FD}}(R)$.

In the region $R \geq 9.2$ fm, the number of the transferred protons is practically zero, while the number of the transferred neutrons slowly increases to the value of around 0.4 as the two nuclei approach each other.
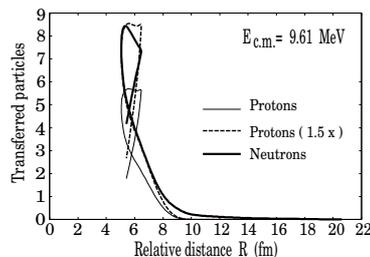

Figure 6: Transferred numbers of the protons (thin curve) and neutrons (thick curve) with respect to the relative distance along the trajectory with the energy $E_{\mathrm{c.m.}} = 9.61$ MeV. The broken curve is plotted by multiplying the number of the transferred protons by a factor of 1.5.

In Fig. 7, the energy of the system is below the top energy of the potential

10

curve $V_{\mathrm{FD}}(R)$. The numbers of the transferred nucleons are small along the trajectory in which the system approaches each other, stop at the turning point, and separate again into two fragments.
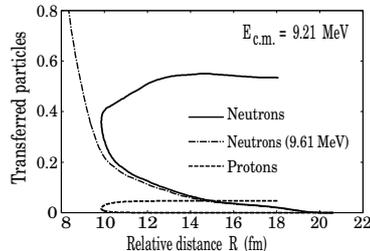

Figure 7: Transferred numbers of the protons (broken curve) and neutrons (solid curve) with respect to the relative distance in the trajectory with the energy $E_{\mathrm{c.m.}} = 9.21$ MeV. The chain curve is for the transferred number of the neutrons in Fig. 6 as a reference.

The number of the transferred protons increase only when the system is near the turning point, though it is much smaller than that of the neutrons under the influence of the Coulomb potential.

The number of the transferred neutrons increases monotonously up to 0.2 as the two nuclei approach each other before they come to the turning point $R \sim 10.0$ fm. The number of the transferred neutrons jumps up by 0.2 near the turning point, and comes up to 0.55 at the end point of the curve in Fig. 7 at the distance $R \sim 18$ fm. As a result, the transferred number of the neutrons is more than ten times as large as that of the protons in the whole process in Fig. 7. The ratio is much larger than the N/Z ratio 1.5 in the ^{20}O. The Coulomb barrier is the main reason for the difference between the transferred numbers of the protons' and that of the neutrons'.

In Fig. 7, we also note that the curve of the transferred neutrons of the trajectory with the energy $E_{\mathrm{c.m.}} = 9.21$ MeV follows that of the trajectory with the energy $E_{\mathrm{c.m.}} = 9.61$ MeV in Fig. 6 in the approaching stage of the two nuclei before they come to the region near the turning point. This could be understood from the variations of the pairing energies in Fig. 5: We see that the pairing energies of the trajectories of the three cases of the energies are kept practically constant at the initial values during the two nuclei approach each other. The tail parts of the neutron densities of the approaching nuclei ^{20}O's with the same pairing energies are almost the same to each other. Then, the transferred numbers of the neutrons during the approaching stage of the two nuclei could be in the common tendency among the three cases of the energies.

11

4 Effects of the initial relative gauge angle

In the superfluid nuclei which satisfy the HFB equations (9), it is well known that there is a gauge invariance in relation with the transformation in terms of an operator $G(\chi) = e^{-i\chi\hat{N}}$ with the number operator $\hat{N}$. The operator $G(\chi)$ transforms the matrices $U_{\alpha k}$ and $V_{\alpha k}$ to $e^{-i\chi}U_{\alpha k}$ and $e^{i\chi}V_{\alpha k}$, respectively. The transformation does not change the properties of the nucleus in the ground state as long as an isolated nucleus is under consideration. In the collision process of the two superfluid nuclei, however, we do not know in advance the effects of the gauge transformations in the two nuclei at the initial time on the properties of the colliding two nuclei on the trajectory.

From the quantum mechanical point of view, the degree of of freedom of the transformation by the operator $G(\chi)$ is made use of to project out a state with a specified number of particles from the HFB state.

In the framework of the mean-field of the (TD)HFB, what we would like to study is the influence of the gauge transformations within the HFB ground states at the initial stage of the colliding nuclei on the behavior of the system later in the collision process.

4.1 A combination of the ^{16}O and ^{20}O

As an example of the case in which the gauge transformation of the superfluid nucleus plays no effects on the collision process, we take the combination of the ^{16}O and ^{20}O. We adopt the phase factors $e^{i\chi}$ with $\chi = 0, 45, 90$, and 135 degrees as the representation of the gauge transformation in the superfluid nuclei ^{20}O,

$$U_{\alpha k} = e^{i\chi}U_{\alpha k}^{(0)}, \qquad V_{\alpha k} = e^{-i\chi}V_{\alpha k}^{(0)}. \tag{26}$$

The ^{16}O is not in the superfluid phase but in the normal state on both sides of the protons and neutrons. Note that this transformation keeps unchanged the normal density, and modify the pairing tensor κ with a phase shift 2χ. In consequence the values of χ between 180 and 360 degrees are redundant with the values between 0 and 180 degrees.

We put the ^{16}O as the left-hand side nucleus and the ^{20}O with the phase factors in Eq. (26) as the right-hand side nucleus in the initial conditions (10) and (11). In the case of the energy $E_{\text{c.m.}} = 11.41$ MeV, the trajectories are shown in Fig. 8, with the different initial gauge angles $\chi = 0, 45, 90$, and 135 degrees. All of the trajectories in Fig. 8 with different initial gauge angles overlap each other completely.

The variations of the pairing energies with respect to the relative distance are shown in Fig. 9 in the cases of the different initial gauge angles χ. After passing the region of the top of the potential energy at $R \sim 8.5$ fm the pairing energies smoothly decrease to - 2 MeV and oscillate about the value. Again, the curves of the pairing energies with different initial gauge angles overlap each other completely.

Thus, we see that there is no dependence on the initial gauge angles in the collision process of the combination of a nucleus in the normal state and
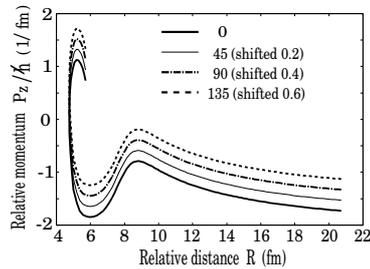
Figure 8: Trajectories of the head-on collisions of the ^{16}O and the ^{20}O with the energy $E_{\text{c.m.}} = 11.41$ MeV in the phase space of the relative distance R and relative momentum P_z. The solid (thin solid, chain, and broken) curve is for the case with the initial gauge angle $\chi = 0$ (45, 90, and 135) degree(s), respectively. All of the trajectories overlap each other. The curve with $\chi = 45$ (90, 135) degrees is shifted upward by 0.2 (0.4, 0.6) 1/fm for the ease of the eyes, respectively.

a superfluid nucleus. This result can be understood simply from the fact that the normal nucleus does not break the gauge angle symmetry. In consequence, changing the phase of the superfluid nuclei is equivalent to changing the whole phase of the system, in which transformation the evolution of the observables is kept unchanged.

4.2 A combination of the ^{20}O and ^{20}O

In the case of the combination of the ^{20}O and ^{20}O, we follow the way of setting the initial condition of the TDHFB equations which is stated in the previous subsection for the case of the collisions of the ^{16}O and the ^{20}O. The initial phase factors $e^{i\chi}$ with $\chi = 0, 45, 90$, and 135 degrees are multiplied on the HFB solutions $U_{\alpha k}^{(0)}$ and $V_{\alpha k}^{(0)}$ of the ground state of the ^{20}O just as in (26). Then each of the set of the matrices $e^{i\chi}U_{\alpha k}^{(0)}$ and $e^{-i\chi}V_{\alpha k}^{(0)}$ are mapped as the right-hand side nucleus, while the HFB solutions $U_{\alpha k}^{(0)}$ and $V_{\alpha k}^{(0)}$, which is just the case with the gauge angle $\chi = 0$, are mapped as the left-hand side nucleus.

In Figs. 10 and 11, we show the trajectories in the case of the energy $E_{\text{c.m.}}$ = 11.41 MeV. The latter figure Fig. 11 is a magnification of the region with the relative distance 4 fm $\leq R \leq$ 11 fm in the former figure Fig. 10.

In contrast to the cases of the combination of the ^{16}O and the ^{20}O in the previous subsection, the trajectories are dependent on their initial gauge angles and are separated from each other in the region of the relative distance $R \leq$ 10 fm. The shift of the trajectory with the initial gauge angle $\chi = 90$ degrees from the one with the angle $\chi = 0$ degree is the largest. The trajectories with the angles $\chi = 45$ and 135 degrees overlap each other and come in the space between the trajectories with the angles $\chi = 0$ and 90 degree(s).
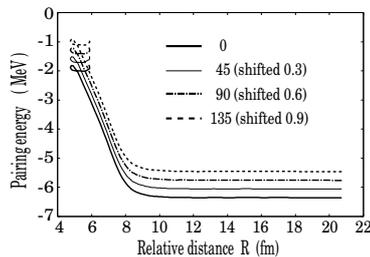
13

Figure 9: Variations of the pairing energies with respect to the relative distance in the collision processes in Fig. 8. The solid (thin solid, chain, and broken) curve is for the case with the initial gauge angle $\chi = 0$ (45, 90, and 135) degree(s), respectively. All of the curves overlap each other. The curve with $\chi = 45$ (90, 135) degrees is shifted upward by 0.3 (0.6, 0.9) MeV for the ease of the eyes, respectively.

Just as in the cases of the trajectories, the variation of the pairing energy with respect to the relative distance R changes as the gauge angle χ is varied. In Fig. 12, we plot the pairing energies of the trajectories in Fig. 11 with respect to the relative distance R with the initial gauge angles $\chi = 0, 45, 90$, and 135 degrees. The size of the shift of the pairing energy with the gauge angle $\chi = 90$ degrees from that with $\chi = 0$ degree is the largest among the three cases of the gauge angles.

In Figs. 13 and 14, we show the trajectories in the case of the energy $E_{\mathrm{c.m.}} = 9.21$ MeV. The latter figure Fig. 14 is a magnification of the region with the relative distance 9.8 fm $\leq R \leq 11$ fm in the former figure Fig. 13.

Just in the same way as the case with the energy $E_{\mathrm{c.m.}} = 11.41$ MeV, the trajectories are dependent on the initial gauge angles χ, and the shift of the trajectory with the angle $\chi = 90$ degrees from that with the angle $\chi = 0$ is the largest. The two trajectories with the angles $\chi = 45$ and 90 degrees overlap each other.

A remarkably different point in the trajectories with the energy $E_{\mathrm{c.m.}} = 11.41$ MeV and $E_{\mathrm{c.m.}} = 9.21$ MeV is as follows: In the case of the energy $E_{\mathrm{c.m.}} = 11.41$ MeV, the point of the relative distance at which the relative momentum P_z of the trajectory takes the smallest absolute value just before the fusion shifts to the direction of the small value of the R when the initial gauge angle is varied from 0 to 90 degrees through 45 degrees. On the other hand, in the case of the energy $E_{\mathrm{c.m.}} = 9.21$ MeV, the turning point of the trajectory shifts toward the large value of the R when the gauge angle is varied as $\chi = 0, 45$, and 90 degrees.

The difference could be understood from the change of the shapes of the frozen density potential energies with respect to the relative distance R when the gauge angle χ is varied. In Fig. 15, we plot the frozen density potential energy curves near the point $R = 9$ fm with the gauge angles $\chi = 0, 45, 90$, 135 degrees. We see that the top of the energy curve shifts to the direction
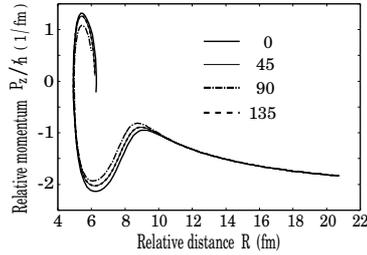
14

Figure 10: Trajectories of the head-on collisions of the ^{20}O and the ^{20}O with the energy $E_{\text{c.m.}} = 11.41$ MeV in the phase space of the relative distance R and relative momentum P_z. Each of the trajectories is the result of the first 2000 steps of the time integration of the TDHFB equations (4). The solid (thin solid, chain, and broken) curve is for the case with the initial gauge angle $\chi = 0$ (45, 90, and 135) degree(s), respectively. The trajectories with the initial gauge angles $\chi = 45$ and 135 degrees overlap each other.
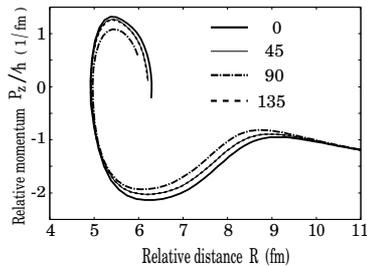
Figure 11: Magnification of the region of the relative distance $R \leq 11$ fm in Fig. 10.

of the small value of the R when the gauge angle is varied as $\chi = 0, 45, 90$ degrees. This is consistent with the shift of the point of the R at which the relative momentum P_z takes the minimum absolute value in the case of the energy $E_{\text{c.m.}} = 11.41$ MeV. Together with the shift of the tops of the frozen density potential energy curves, they are shifted upward when the gauge angle is varied as $\chi = 0, 45,$ and 90 degrees. Then, the section point of the potential energy curve with the energy $E_{\text{c.m.}} = 9.21$ MeV shifts toward the large value of the R. This is consistent with the shift of the turning points of the trajectories in Fig. 14 with the angles $\chi = 0, 45,$ and 90 degrees.

To understand this phenomena, we can look at the total energy in the frozen calculation that is directly related to the nucleus-nucleus potential in Fig. 15. Because the normal density is not affected by the relative phase, only the pairing
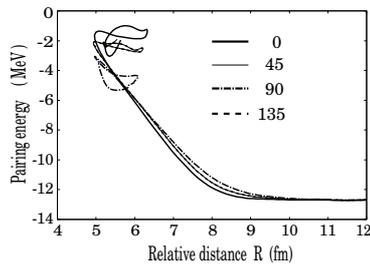
Figure 12: Variation of the pairing energies with respect to the relative distance R in the trajectories in Fig. 11.
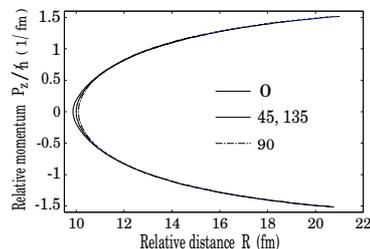

Figure 13: Trajectories of the head-on collisions of the ^{20}O and the ^{20}O with the energy $E_{\text{c.m.}} = 9.21$ MeV in the phase space of the relative distance R and relative momentum P_z. The solid (chain) curve is for the case with the initial gauge angle $\chi = 0$ (90) degree(s), respectively. The thin solid curve is for both $\chi = 45$ and 135 degrees. The trajectories with the angles $\chi = 45$ and 135 degrees overlap each other.

part of the total energy changes with the choice of the relative gauge angle,

$$E_{\text{pair}} = \frac{1}{4} \sum_{\alpha\beta\gamma\delta} \overline{v}_{\alpha\beta\gamma\delta} \kappa^*_{\alpha\beta} \kappa_{\gamma\delta}. \tag{27}$$

The κ matrix can be decomposed into a part coming from the left nuclei and a part coming from the right. Because the phase of the κ coming from the right part is shifted by a phase 2χ, the total κ matrix is expected to be minimum for the angle $\chi = 90$ degrees. This phase dependence of the potential energy illustrates that the nucleus-nucleus interaction energy for $\chi = 90$ degrees is smaller than that for $\chi = 0$. Here, the nucleus-nucleus interaction energy is the difference between the Coulomb energy and the frozen density potential energy at each point of the relative distance R.

Let us pay attention to the behaviors of the variations of the number of the neutrons in the left region. The left and right regions are separated by a section plane located at $z = z_s$ that is introduced in Section III.
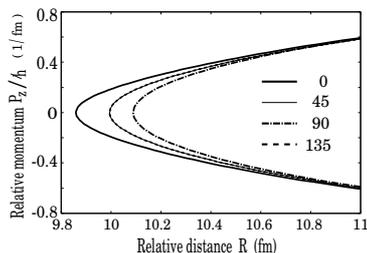
16

Figure 14: Magnification of the region of the relative distance 9.8 fm $\leq R \leq$ 11 fm in Fig. 13. The solid (thin solid, chain, and broken) curve is for the case with the gauge angle $\chi = 0$ (45, 90, and 135) degree(s), respectively.
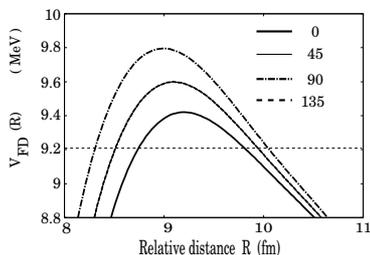

Figure 15: The frozen density potentials $V_{\mathrm{FD}}(R)$ with respect to the relative distance R with the initial gauge angle $\chi = 0$ (solid), 45 (thin solid), 90 (chain), and 135 (broken) degrees. The thin broken line stands for the energy $E_{\mathrm{c.m.}} = 9.21$ MeV.

In Figs. 16 and 17, we show the variations of the numbers of the neutrons with respect to the relative distance R when the gauge angle is varied as $\chi = 0$, 45, 90, and 135 degrees. Each of the curves in the figures stands for the difference of the number N_{L} of the neutrons in the left region from the initial value 12. The N_{L} is calculated just like Eq. (18) with $\rho(\mathbf{r})$ replaced by the neutron density $\rho^{(n)}(\mathbf{r})$,

$$N_{\mathrm{L}} = \int d^3x \; \rho^{(n)}(\mathbf{r})\theta(z_{\mathrm{s}} - z) \,. \tag{28}$$

In both of the figures, the curves for the gauge angles $\chi = 0$ and 90 degrees are flat, denoting that the numbers of the neutrons in the left region are kept to be 12 all along the trajectories. In the cases of the trajectories with the gauge angles $\chi = 45$ and 135 degrees, on the other hand, the number of the neutrons increase (decrease) for the gauge angle $\chi = 45$ (90) degrees in the left region, respectively.

In Fig. 17, we see that the change of the number N_{L} of the neutrons is realized near the turning point of the trajectory of the bouncing nuclei. When
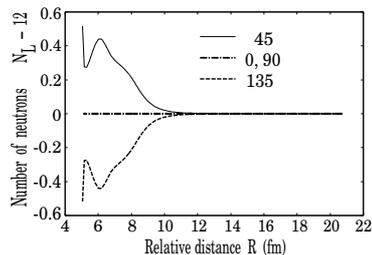
17

Figure 16: Variation of the number N_{L} of the neutrons in the left region with respect to the relative distance R with the energy $E_{\mathrm{c.m.}} = 11.41$ MeV. The thin solid (broken) curve is for the case with the gauge angle $\chi = 45$ (135) degrees, respectively. The chain curve is for the cases with $\chi = 0$ and 90 degrees. The two curves of the cases with $\chi = 0$ and 90 degrees overlap each other.
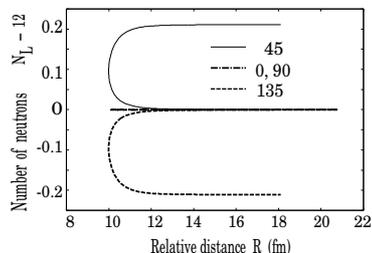

Figure 17: The same as in Fig. 16, but for the energy $E_{\mathrm{c.m.}} = 9.21$ MeV.

the number N_{L} of the neutrons is plotted with respect to the elapsed time in Fig. 18, the smooth variation of the number N_{L} is clearly illustrated. Thus, the figures 16 to 18 suggest us the dependence of the number N_{L} on the relative gauge angle $\Phi = 2\chi$ with the periodicity 2π.

Taking account of the one-dimensional situation of the present calculations of the head-on collisions, and assuming the 2π periodicity of the number N_{L} of the neutrons in the left region with respect to the relative gauge angle Φ, we guess that the flux J_{s} of the neutrons across the section plane at $z = z_{\mathrm{s}}$ is proportional to the sine of the angle Φ,

$$J_{\mathrm{s}} \propto \sin\left(\Phi\right). \tag{29}$$

The relation in (29) reminds us the Josephson current of the electron pair through the Josephson junction with a relative phase Φ of the two superconducting objects separated by a thin insulator [23, 24]. The detailed studies are needed to understand the microscopic background of the flows of the nucleons under the condition of the superfluidity illustrated in the figures 16 to 18.
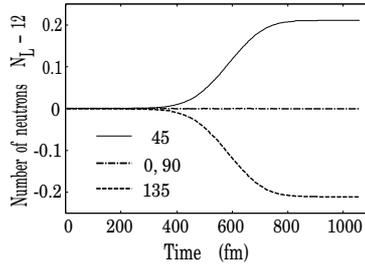
18

Figure 18: The same as in Fig. 17, but the variations of the number N_L of the neutrons in the left region are plotted with respect to the elapsed time.

5 Summary and concluding remarks

In this article, we have reported the first results of the application of the method of solving the TDHFB equations with the Gogny force to the head-on collision processes of the superfluid nuclei ^{20}O $+$ ^{20}O. The method of solving the TDHFB equations are realized by using the two-dimensional harmonic oscillator eigenfunctions and one-dimensional Lagrange mesh [21]. A candidate of the way of setting up the initial conditions of the collision processes was proposed.

The advantage of the present numerical method is the natural cut-off for quasi-particle energy obtained by using a Gaussian type finite range interaction. Furthermore, the choice of the present hybrid basis allows to include all the quasi-particle states, then the unitarity relations (12) to (15) are respected during the evolution. These two points are expected to contribute to the stable numerical integrations of the TDHFB equations.

Setting the energies of the colliding nuclei around the energy of the top of the frozen density potential energy, we have displayed the trajectories, variations of the pairing energies with respect to the relative distance, and the numbers of the transferred nucleons.

We studied the effects of the initial relative phase on the properties of the colliding superfluid nuclei. In particular, the dependence of the trajectories, pairing energies, and transferred number of the neutrons on the relative phase was visually illustrated in the figures. We showed that the static and dynamical nucleus-nucleus potential depends on the relative gauge angle between two superfluid nuclei. For the reaction ^{20}O $+$ ^{20}O the difference concerning the potential energy is about 0.4 MeV for the height of the barrier and 0.2 fm for the position of the barrier.

Some remarks concerning the present calculations are as follows:

1. The set up the initial conditions of the TDHFB equations of the colliding superfluid nuclei was of a *sharp cut-off* type, by assuming that the correlations of the two nuclei at the initial time could be neglected when they were set apart with large distance. At present, the effects of the sharp cut-off initial conditions have not been studied. It would be interesting to compare the results

19

of the present calculations with those obtained by using other types of initial conditions.

2. In all of the numerical calculations in this article, we have used a fixed set of the parameters of the basis functions (number of the grid points N_{grid}, grid size Δz, maximum number of the two-dimensional harmonic oscillator shell N_{shell}, and harminic oscillator frequency $\hbar\omega$, and so on). The dependence of the numerical results on the parameters of the basis functions will be studied before the heavier nuclei are treated in the future calculations.

3. In calculating the numbers of the transferred nucleons, we followed Washiyama's method proposed in the TDHF framework. It would be necessary to study the present results from the quantum mechanical viewpoint by making use of the number projection method [22].

4. The present contribution shows that there is a dependence of the observables with respect to the initial gauge angle. Nevertheless, the two fragments should initially respect the gauge angle symmetry and preserve the initial good number of particles in each fragments. It would be interesting for future applications to develop a self-consistent time-dependent mean-field theory that describes the evolution of a quasi-particle state projected on the good number of particles.

The transfer mechanism of the nucleons in the collision processes of the superfluid nuclei will be studied in a future analysis by combining the present method of solving the Gogny-TDHFB equations with the quantum mechanical method of the number projection [22].

Acknowledgment

References

[1] A. Bohr and B. R. Mottelson, Nuclear Structure (Benjamin, New York, 1975).

[2] P. Ring and P. Schuck, The Nuclear Many-Body Problems (Springer-Verlag, 1980).

[3] R. A. Broglia and A. Winther, Heavy Ion Reactions (Westview Press, Boulder, 2004).

[4] G. Scamps, C. Simenel, and D. Lacroix, Phys. Rev. C 92, 011602(R) (2015).

[5] A. Bulgac, P. Magierski, K. J. Roche, and I. Stetcu, Phys. Rev. Lett. 116, 122504 (2016).

[6] P. Bonche, S. Koonin, and J. W. Negele, Phys. Rev. C13, 1226 (1976).

[7] J. W. Negele, Rev. Mod. Phys. 54, 913 (1982).

[8] J. A. Maruhn, K. T. R. Davies, and M. R. Strayer, Phys. Rev. C 31, 1289 (1985).

[9] A. S. Umar, M. R. Strayer, R. Y. Cusson, P. G. Reinhard, and D. A. Bromley, Phys. Rev. C 32, 172 (1985).

[10] T. Nakatsukasa and K. Yabana, Phys. Rev. C 71, 024301 (2005).

[11] A. S. Umar and V. E. Oberacker, Phys. Rev. C 74, 021601(R) (2006).

[12] K. Washiyama and D. Lacroix, Phys. Rev. C 78, 024610 (2008).

[13] A. S. Umar, V. E. Oberacker, J. A. Maruhn, and P. G. Reinhard, Phys. Rev. C 80, 041601 (2009).

[14] D. J. Kedziora and C. Simenel, Phys. Rev. C 81, 044613(2010).

[15] C. Simenel and A. S. Umar, Phys. Rev. C 89, 031601(R) (2014).

[16] Y. Hashimoto and K. Nodeki, arXiv:0707.3083 [nucl-th] (2007).

[17] B. Avez, C. Simenel, and P. Chomaz, Phys. Rev. C 78, 044318 (2008).

[18] S. Ebata, T. Nakatsukasa, T. Inakura, K. Yoshida, Y. Hashimoto, and K. Yabana, Phys. Rev. C 82, 034306 (2010).

[19] I. Stetcu, A. Bulgac, P. Magierski, and K. J. Roche, Phys. Rev. C 84, 051309 (2011).

[20] Y. Hashimoto, Eur. Phys. J. A 48, 55 (2012).

[21] Y. Hashimoto, Phys. Rev. C 88, 034307 (2013).

[22] G. Scamps and D. Lacroix, Phys. Rev. C 87, 014605 (2013).

[23] B. D. Josephson, Phys. Lett. 1, 251 (1962).

[24] B. D. Josephson, Rev. Mod. Phys. 36, 216 (1964).

[25] V. I. Goldanski and A. I. Larkin, Sov. Phys. JETP 26, 617 (1968).

[26] K. Dietrich, Phys. Lett. 32B, 428 (1970).

[27] K. Dietrich, Ann. Phys. 66, 480 (1971).

[28] K. Dietrich, K. Hara, and F. Weller, Phys. Lett. 35B, 201 (1971).

[29] M. Kleber and H. Schmidt, Z. Physik 245, 68 (1971).

[30] R. A. Broglia, Ann. Phys. 80, 60 (1973).

[31] C. Simenel, Phys. Rev. Lett. 105, 192701 (2010).

[32] K. Sekizawa and K. Yabana, Phys. Rev. C 88, 014614 (2013).

[33] K. Sekizawa and K. Yabana, Phys. Rev. C 90, 0646142014).

[34] D. Baye and P. Heenen, J. Phys. A 19, 2041 (1986).

[35] T. Matsuse, RIKEN Review 19, 18 (1998).